

TIME-DOMAIN MEASUREMENTS AND MODELING OF UXO

Robert E. Grimm, Ph.D.
Blackhawk Geoservices, Inc.
301 B Commercial Rd.
Golden, CO 80401
Voice: 303-278-8700
Fax: 303-278-0789
Email: grimm@blackhawkgeo.com

Category: Session 38, Testing of Systems and Technology

Abstract

A commercial finite-element engineering-analysis code was used to model pulsed-induction (time-domain) sensing of UXO for comparison with measurements made with the Geonics EM61-3D. Late-time decay constants are observed to be independent of shape and orientation in solid nonpermeable (aluminum) objects with the same volume, in agreement with theory, except for flattened objects on end with respect to the primary field. Solid permeable (steel) objects are strongly influenced by the amount of metal inline with the primary field. Hollow interiors are manifested as a straight-line semilog decay, indicating that the eddy-current system has collapsed to a single mode. The time until collapse is given by the diffusion time through the wall thickness. Complexly shaped, material-composite UXO show complex eddy-current patterns, but the measured magnetic field or voltage is dominated by polarization in steel portions of the target. In an 81-mm projectile, for example, strong eddy currents circulate in the fin shroud in early time and decay rapidly, but a model without the fin shroud showed little difference in receiver voltage. Large magnetic inductions are present in the permeable steel body in both models and decay slowly, supported only by small eddy currents. Although there are some shifts in the loci of maximum induction, the generally smooth penetration and decay of magnetic fields in the target accounts for the relative success of simple analytic and empirical models in reproducing EM measurements of ferrous UXO.

Introduction

Electromagnetic (EM) induction sensors have been recognized as a principal means of UXO detection and likely discrimination. The Geonics EM61 and other popular metal detectors measure a single time gate or frequency of the secondary currents induced in a target. In geological EM exploration, the proven approach to best describing target size, shape, and orientation is to use multiple time gates and all three spatial components of the secondary field. The Geonics EM61-3D is a multicomponent, multichannel pulsed-EM induction sensor designed to bring these capabilities to UXO discrimination. Previous work with the EM61-3D and related prototypes are described by *McNeill and Bosnar (1996)* and *Grimm et al. (1997)*. The recently introduced Geonics EM63 measures a comparable time range but eliminates recording the horizontal spatial components in favor of higher signal-to-noise for the vertical component. The EM61 MkII also measures the only vertical component in a more restricted number of time

gates. We have performed numerous field and test-bed measurements with the EM61-3D and are presently investigating three approaches to modeling the data: (1) a parameterized curve fit commonly used by UXO researchers, (2) a semianalytical theory that approximates targets as solid ellipsoids of revolution, and (3) finite-element numerical methods. Here we report preliminary application of finite elements to model the time-domain EM response of several idealized target shapes and one realistic projectile.

Finite-Element Model

Within the UXO community, numerical methods are being investigated by the Duke (L. Carin) and CRREL (K. O'Neill) groups. Both use customized legacy codes developed in-house. However, commercial packages are widely available for multiphysics engineering design, including both frequency- and time-domain EM induction and propagation. We have begun testing one such package, *ANSYS*, for EM modeling of UXO using the finite-element method (FEM). We have previously used the structural, fluid-dynamics, and low-frequency EM portions of *ANSYS* to model geodynamic deformation, hydrothermal systems, and planetary induction, respectively.

The solution selected from *ANSYS* for this problem uses the node-based, three-dimensional magnetic vector potential (MVP). This approach is known to be inaccurate at discontinuities in permeability, and hence an alternative edge-based MVP formulation is recommended (ANSYS, 1998). However, *ANSYS* does not support an “infinite boundary element” for the latter, which would require modeling a large air volume around the sensor and target to eliminate artificial reflections. Instead, a workaround was used for the node-based solution (*Bulat et al.*, 1998). The workaround consists of creating a model in which the boundary between the permeable and surrounding nonpermeable domains is discontinuous, i.e., pairs of coincident nodes exist on the interface. Nodal rotation is then used so that 2 of the 3 nodal directions of each boundary node are tangent to interface. Coupling the tangential components of the MVP between coincident pairs of nodes on the boundary and leaving the normal component uncoupled largely eliminates the error that would exist if the model were contiguous. These results have been verified by comparison with 2D axisymmetric models, which do not have the permeability-boundary error. The solutions agree to within a few percent.

Open-domain models like this one would be best treated with the Trefftz method, which combines the efficiency of boundary-element techniques with a finite-element like positive-definite stiffness matrix. At present, unfortunately, *ANSYS* only supports this formulation for electrostatics and not electromagnetics. Indeed, computation in the large number of air elements is the time-limiting part of this analysis. Improved meshing strategies may also improve the computational efficiency and stability.

As the development of the finite-element mesh and loads from a conceptual model can be tedious, a series of macros (command-language programs) were written to speed up this process. For simplicity, only axisymmetric objects are considered at present. The user supplies a meshed half-section of the object with the appropriate material properties (aluminum, steel, or air) assigned. It is important to keep the mesh size in the object rather smaller than the diffusion length per time step. The macros extrude the object to 3D and place it in the desired position and orientation with respect to the sensor. The transmitter coil is explicitly modeled with finite elements and the load (waveform) in them defined. The entire model domain is meshed and the solution is performed in batch processing. The EMF in the receiver coil(s) is computed in post-

processing by taking a numerical time derivative of the contour integral of the MVP along the receiver coil(s). Current density, magnetic induction, and other quantities can be viewed as a function of time using the internal functionality of *ANSYS*.

All of the sensor parameters were originally developed to match the EM61 and have not yet been modified for the EM61-3D at the time of this writing. Therefore the EMF is computed in 1-m receiver coils that are coincident and 0.4-m above the transmitter coil, and not in the 0.4-m coils centered on the transmitter. Furthermore, the transmitter base frequency is 75 Hz (EM61) and not 7.5 Hz (EM61-3D). The difference in frequency content of the transmitter on-ramp may introduce some differences. Finally, there is no accommodation for “previous-pulse” effects; these will be computed later by observing the voltage decay to longer times and summing at each period of the receive gates until the signal is negligible. (Note that, in the frequency domain, this effect is automatically accounted for by the periodicity of the Fourier transform).

Equal-Volume Solid Canonical Objects

A preliminary set of calculations was performed on “canonical” objects, solid ellipsoids of revolution. Three objects were constructed that had the same volume but differed markedly in their aspect ratios: a sphere, a 4:1 prolate ellipsoid of revolution, and a 1:16 oblate ellipsoid of revolution. Each object was alternately tested using the material properties of aluminum ($\mu_r=1$, $\sigma=3.5 \times 10^7$ S/m) and of steel ($\mu_r=200$, $\sigma=0.2 \times 10^7$ S/m). The center of the object was positioned 1 m below the center of the transmitter coil. Two orientations tested: longitudinal, with the symmetry axis parallel to the (vertical) primary field (perpendicular to the plane of the coil), and transverse, with the object’s symmetry axis perpendicular to the primary field (parallel to the plane of the coil). This first round of calculations was performed in quarter-symmetry for better computational efficiency (Fig. 1.)

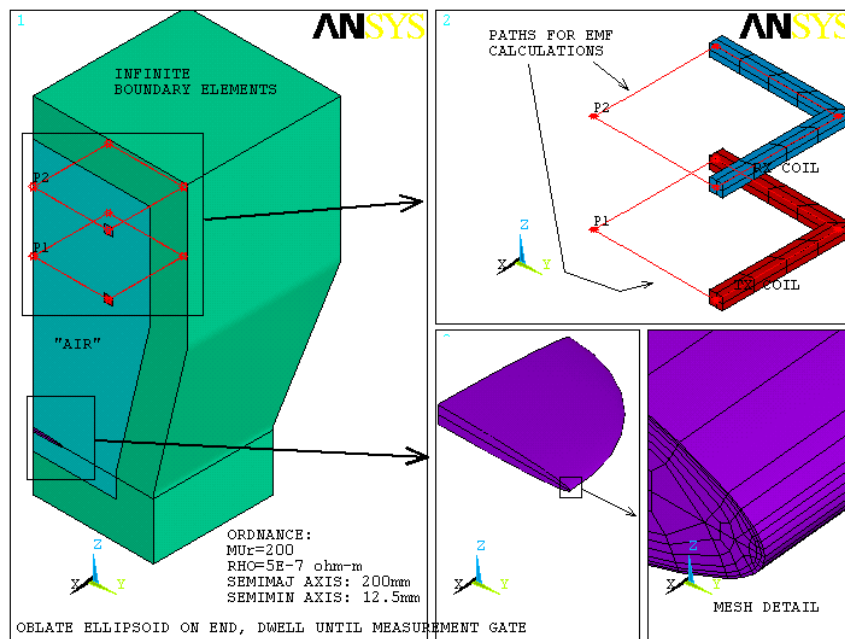


Figure 1. Model domain and mesh detail for one of the ten “canonical-object” (here, OL_s) calculations. Note that the figure on the left is shows only the model geometry, not the mesh.

Table 1. Equal-Volume Solid Canonical Objects

Object	A (mm)	B (mm)	C (mm)	R (mm)
Prolate Ellipsoid	50	50	200	NA
Oblate Ellipsoid	200	200	12.5	NA
Sphere	NA	NA	NA	79.4

Table 2. Solid Canonical Object Test Cases

Case	Shape	Orientation	Material
PL _S	Prolate Ellipsoid	Longitudinal	Steel
PT _S	Prolate Ellipsoid	Transverse	Steel
OL _S	Oblate Ellipsoid	Longitudinal	Steel
OT _S	Oblate Ellipsoid	Transverse	Steel
PL _A	Prolate Ellipsoid	Longitudinal	Aluminum
PT _A	Prolate Ellipsoid	Transverse	Aluminum
OL	Oblate Ellipsoid	Longitudinal	Aluminum
OT _A	Oblate Ellipsoid	Transverse	Aluminum
S _S	Sphere	NA	Steel
S _A	Sphere	NA	Aluminum

Normalized time decays for the aluminum and steel spheres computed analytically and by *ANSYS* are in good agreement overall (Figs. 2a,b). Some error is introduced by spatial and temporal interpolation of the nodal solution, and there also appears to be a discontinuity upon an automatic increase in the time step near 5 ms for the aluminum case.

The time constant τ for late-time eddy-current decay is always proportional to a conductance-length product, i.e., two length scales multiplied by electrical conductivity: $\tau \propto L_1 L_2 \sigma = S L_2$, where S is the conductance. For the sphere, the length scales are both r : $t = \sigma \mu r^2 / \pi^2$. For other nonpermeable objects, the following algorithm may be used to deduce qualitative late-time decay constants (derived from *Kaufman, 1978*, and unpublished Geonics Workshop Notes):

1. The first dimension is always the smallest of the target and is used to form the conductance. This does not have to be in the direction of the incident field.
2. The second dimension is the shorter of the directions perpendicular to the incident field, i.e., the smallest cross-section.

A corollary to these rules is that the late-time decay constant does not depend on the longest dimension.

Therefore the late-time decay constant for OT_A should be proportional to the semiminor axis squared (b^2) and the product of semiminor and semimajor axes (ab) for OL_A; the asymptotic late-time constants are indeed $\mu\sigma ab/4$ and $\mu\sigma b^2/4$, respectively, when $a \gg b$ (*Kaufman, 1978*). The late-time decay constant for both PL_A and PT_A should both be proportional to the semiminor axis squared (b^2), i.e., independent of orientation. No analytic solution is known for the late-time decay of currents in such an object, but a circular cylinder, approximating $b \gg a$, has a decay constant $\mu\sigma a^2/6$ under a transverse primary field.

Neglecting the minor differences in the constant terms, the late-time decay constants should be roughly 1:1:1:(1/16) for the PL_A, PT_A, OL_A, and OT_A targets, respectively. In other words, these two targets with the same volume should have identical late-time decay rates in all orientations, except OT_A, which should decay rapidly. Correcting for the approximate factor of 2 difference in constant terms between the sphere and the ellipsoids, the sphere should have a late-

time decay comparable to the three slow-decaying ellipsoids. All of these semi-quantitative predictions are confirmed by the numerical calculations.

The early-time amplitudes are ranked (in decreasing order) OL_A , PL_A , OT_A , PT_A . The largest currents can be coupled for the disk that is facing the coil (OL_A). PL_A can also take advantage of the symmetry and induce many current rings along its length.

The time decays for the steel targets cover a wider range of amplitudes. The rules of thumb developed above no longer apply because the large magnetic polarizability dominates the response. The PL_S target now has the highest amplitude because it is optimally polarizable, followed by OT_S , OL_S , and PT_S . The high polarizability of the OT_S target quantitatively shows why analyses based on the EM-61 can misidentify plates on end as flat-lying cylinders. However, these results were computed only for targets centered beneath the coils and will change as the coils are moved.

Hollow Sphere

A second investigation was begun to investigate the effects of hollow objects. Two 10-cm diameter steel spheres were considered, one solid and one hollow with a 5-mm thick wall (10% of radius). The objects were placed 0.9 m directly below the transmitter coil (simulated depth 0.5 m).

The receiver voltages for the hollow sphere depart dramatically from those of the solid sphere at about 5 ms (Fig. 3). This occurs as the maximum eddy current completes its diffusion through the shell: the diffusion time is of order $t \sim \sigma \mu d^2$, so the 5-mm steel wall should be traversed in about 13 ms, in order-of-magnitude agreement with the computations. The subsequent voltage decay is semilogarithmic and well-described by a single decay-time constant of 1.6 ms. The currents at this time are largely confined to an equatorial ring. The decay-time constant for a permeable ring (*Kaufman and Keller, 1985*) with diameter equal to that of the sphere and thickness equal to that of the shell, is 5 ms. By comparison, the decay-time constant for a disc with diameter equal to the radius is 22 ms and that for the entire sphere is 140 ms.

81-mm Projectile

The final simulations presented here are representative of those to be performed under a new contract from SERDP. The outline and major components of an 81-mm HE projectile were digitized from drawings (Figs. 5,6). The item consists of solid aluminum nose and tail sections and a hollow steel body. The explosive is considered to be nonconductive and is treated as air. Because we are presently restricted to axisymmetry, the tail fins are neglected, but the fin shroud is simply modeled as a detached ring (Figs. 5,6). The target was placed nose-down 0.9 m directly below the transmitter coil. The predicted time decay compares favorably to EM61-3D data (Fig. 4), although there are some notable early-time discrepancies.

The detailed behavior of eddy currents within the object evolves heterogeneously with time. Just after transmitter turn-off (Fig. 7, left), the tail-fin shroud is “lit up” with the highest eddy-current density. Lesser current densities exist in the tail-boom threads, the base of the fuze, and the tail boom. The smallest current densities are in the steel body itself. At a later time (Fig. 7, right), the tail-shroud currents have completely collapsed because the metal is thin there, and the current system in the tail-boom threads dominates. These currents supported through time because they cannot diffuse effectively into the steel tail-boom screw.

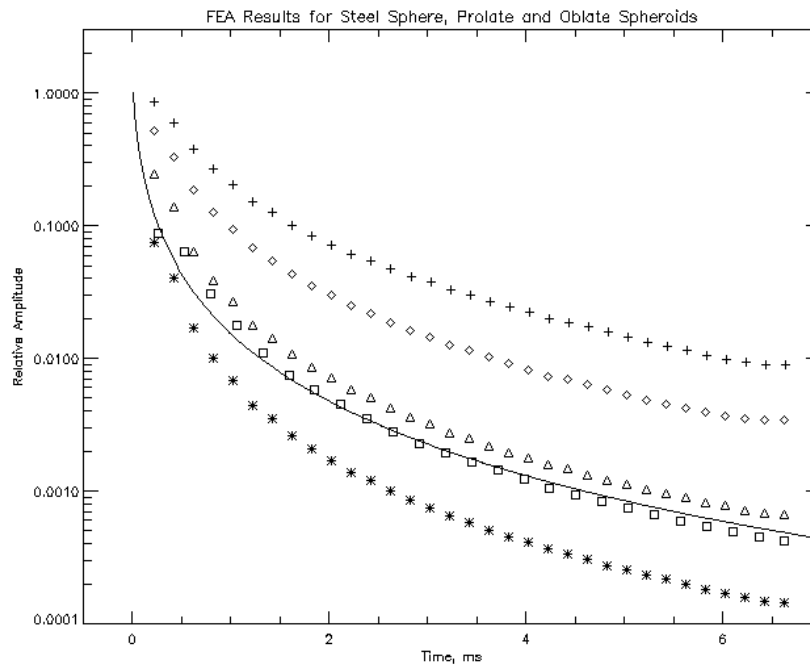
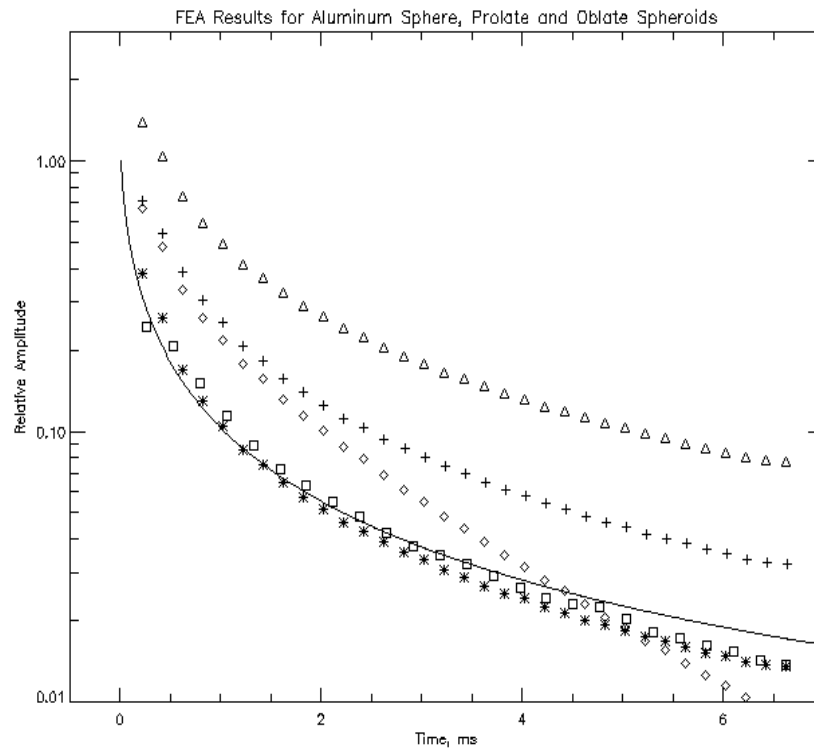
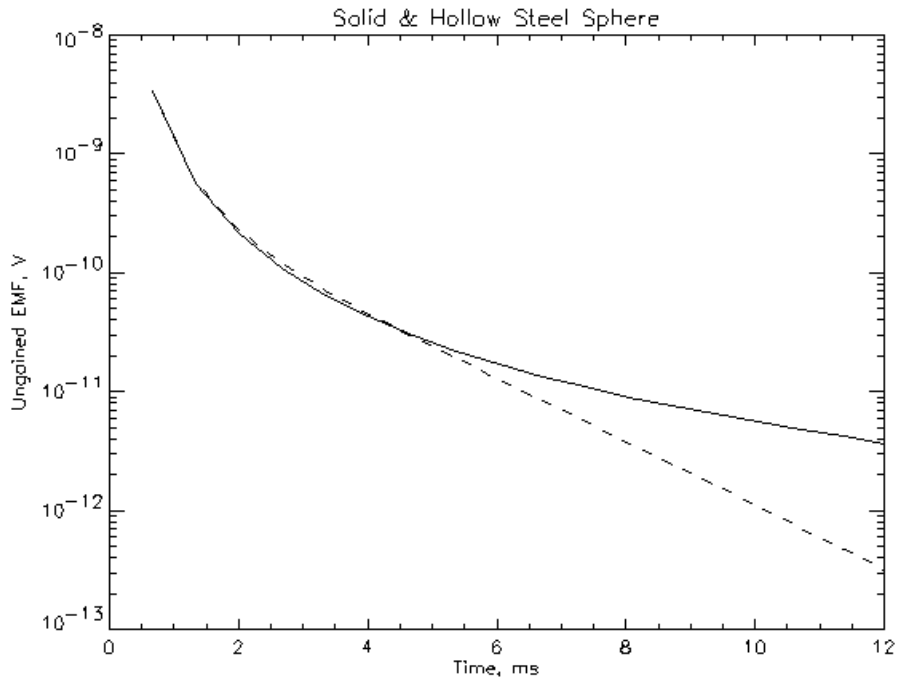


Figure 2. ANSYS finite-element solutions for simulated EM61 response (with expanded time scale) to aluminum objects. Key: PL–crosses; PT–asterisks; OL–triangles; OT–diamonds; sphere–squares; solid line–analytic solution for sphere. Top (a): Aluminum. Bottom (b): Steel



X

Figure 3. EMF in a solid 10-cm diameter steel sphere (solid line) vs. hollow sphere (dashed line). Departure at ~5 ms is comparable to expected diffusion time through the shell and time constant is comparable to that for a ring with thickness equal to that of the shell.

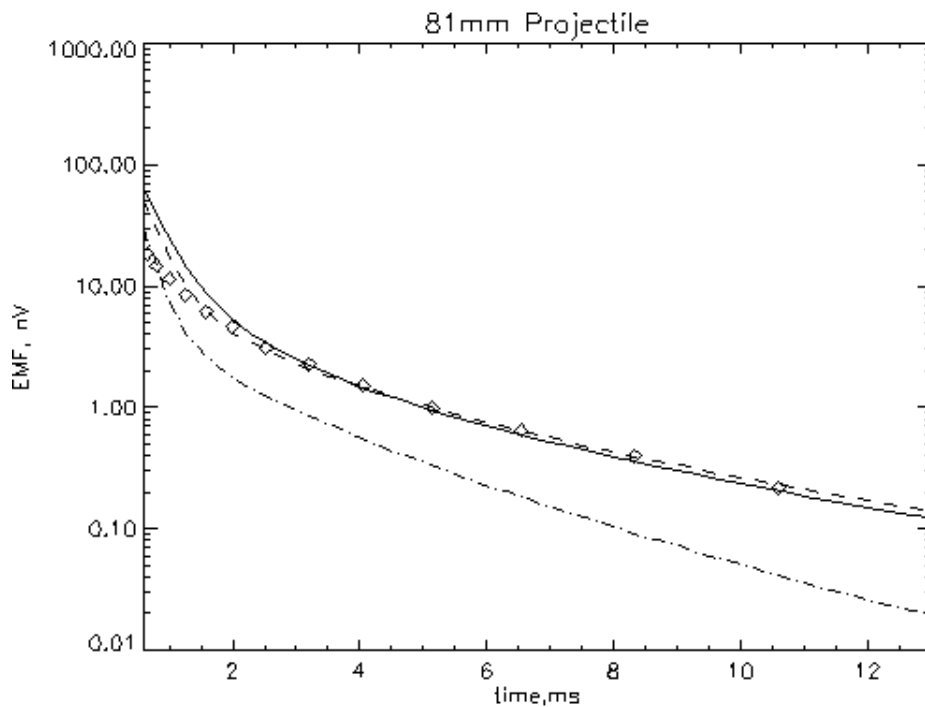


Figure 4. Comparison of simulated EMF (solid line) from nose-down 81-mm projectile vs. EM61-3D measurement (symbols). Early-time discrepancy is likely due to errors in numerical time differentiation of B-field or erroneously higher transmitter base frequency. Same model without tail-fin shroud (dashed line) is practically identical, indicating that most of the signal comes from the steel body and not the tail. Lower amplitude for projectile in horizontal orientation (dot-dash line) is again due to smaller amount of permeable steel in-line with primary magnetic field.

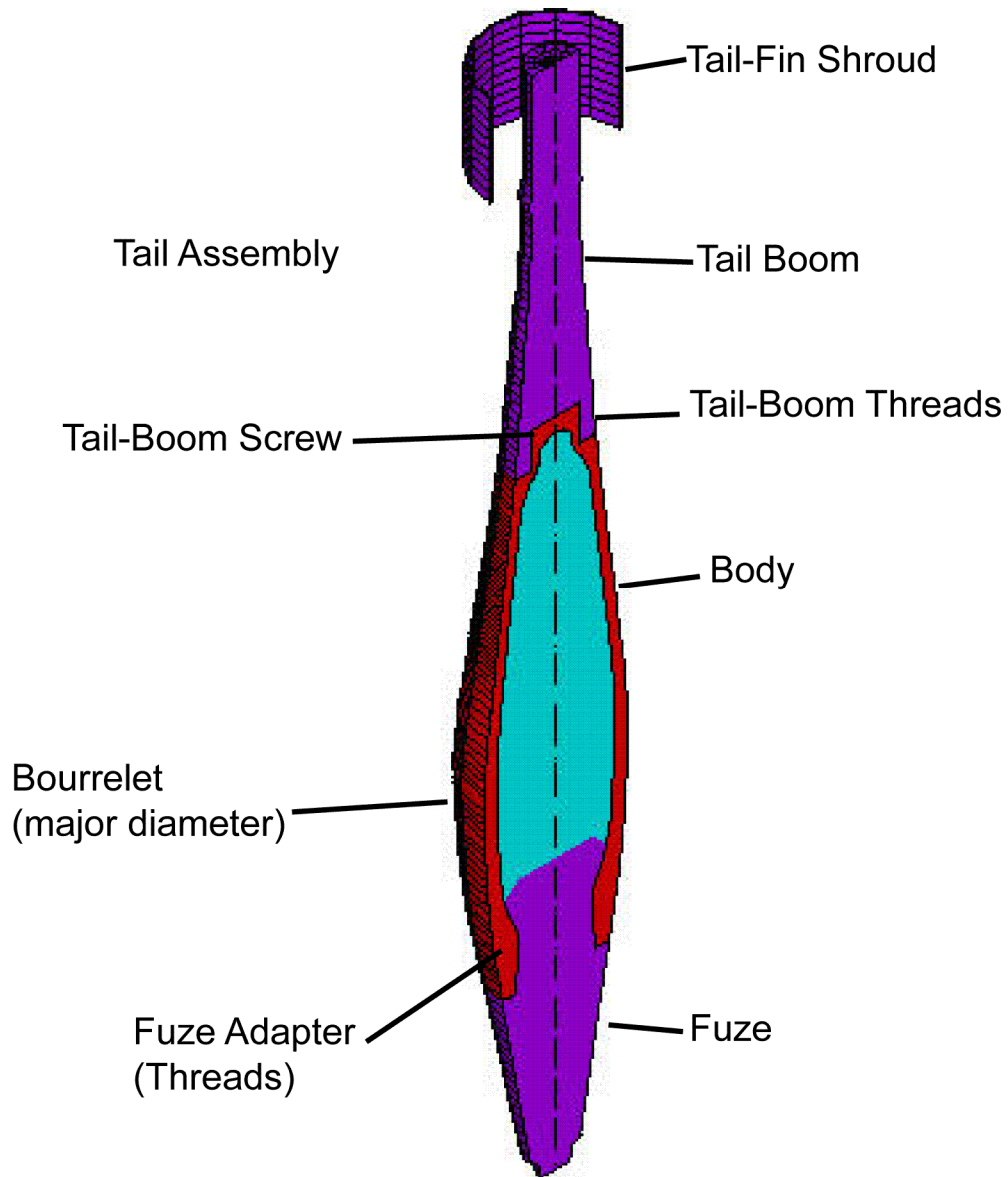


Figure 5. 81-mm projectile anatomy. Red is steel, purple is aluminum, and light blue is “air.”

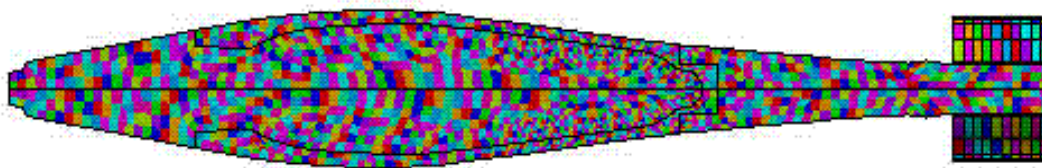


Figure 6. Finite-element discretization of 81-mm projectile.

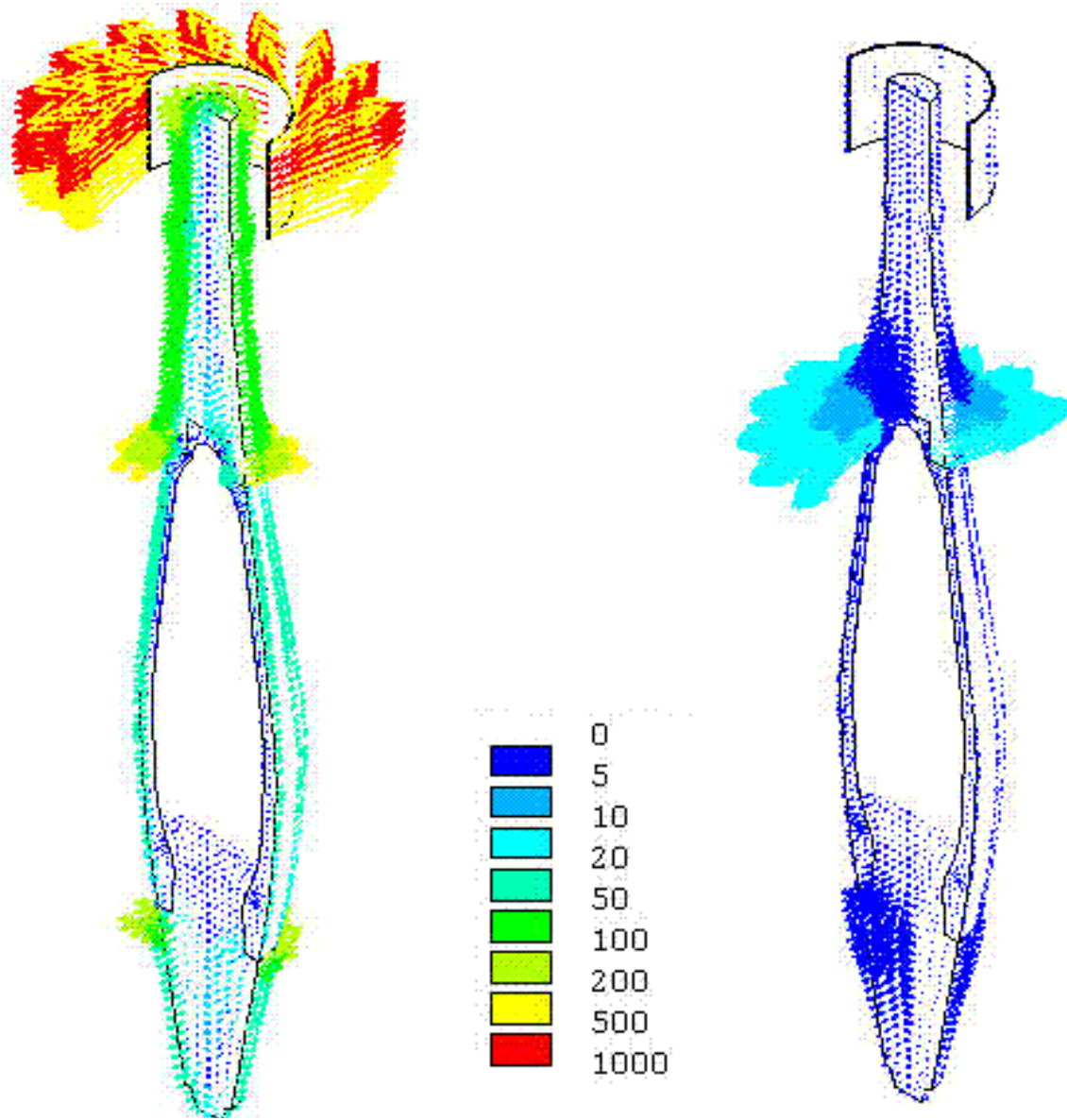


Figure 7. Simulated current density at 0.6 ms (left) and 9.6 ms (right) after transmitter turnoff in nose-down 81-mm projectile. The former corresponds approximately to the EM61 time gate and the latter to the end of the EM61 waveform. Note strong early-time currents in tail-fin shroud and late-time concentration in tail-boom threads. The latter occurs because currents are unable to diffuse into the steel tail-boom screw and are therefore supported to longer times than expected for a simple ring.

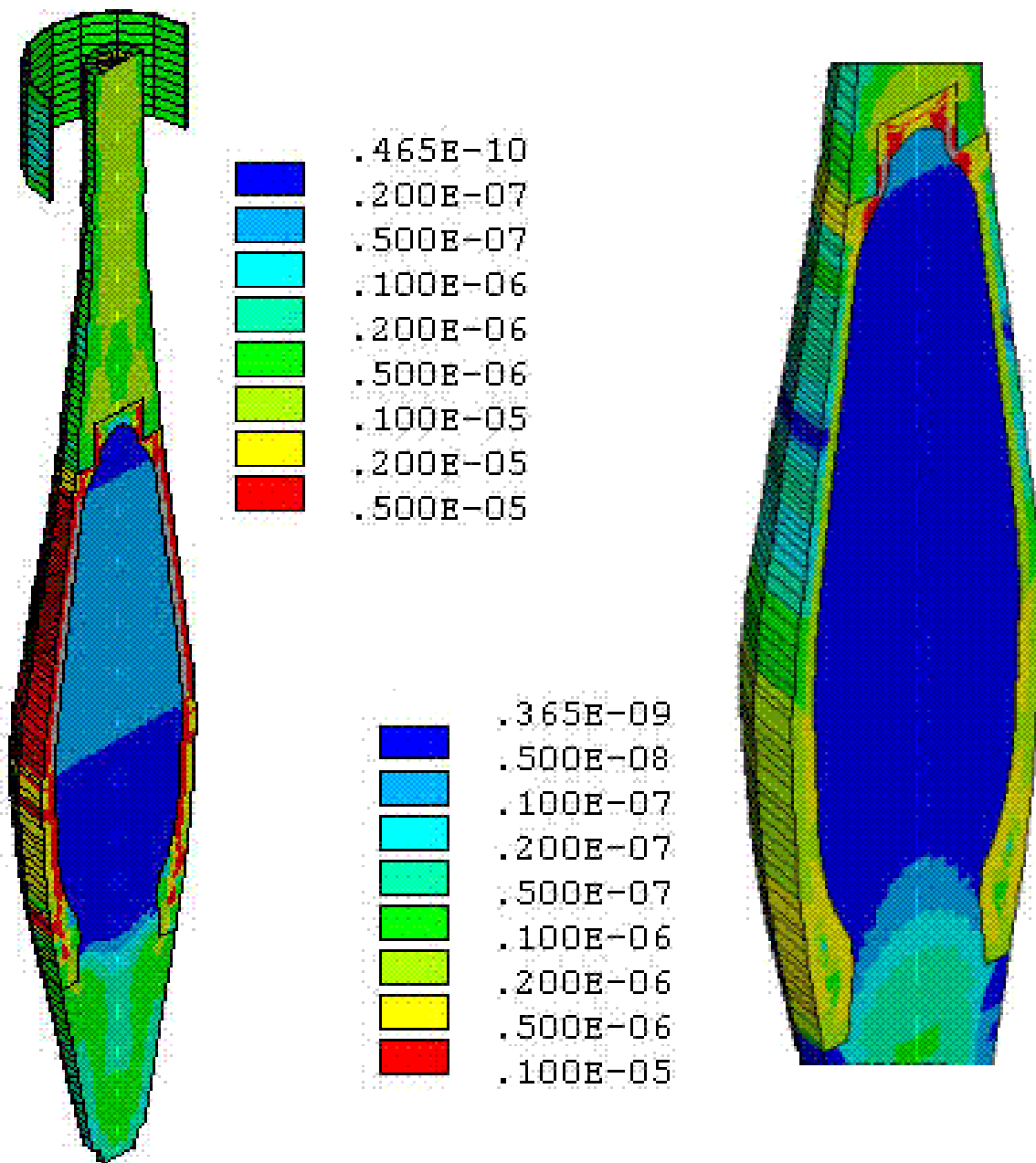


Figure 8. Simulated magnetic induction at 0.6 ms (left) and 9.6 ms (right) after transmitter turnoff in nose-down 81-mm projectile. Grey color in aft part of steel body is off-scale. Largest induction in steel casing decays smoothly with time, with some trend toward concentration in the thickest parts (tail-assembly screw and fuze adaptor).

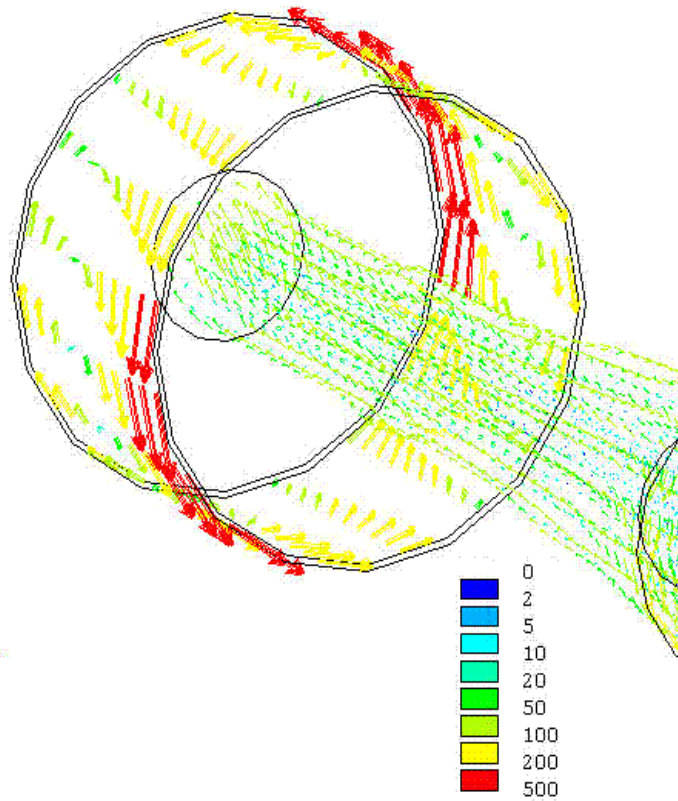


Figure 9. Eddy currents in tail-fin shroud for horizontal 81-mm projectile 0.6 ms after transmitter turnoff. Note asymmetric distribution and countercirculation, indicating excitation of higher-order modes.

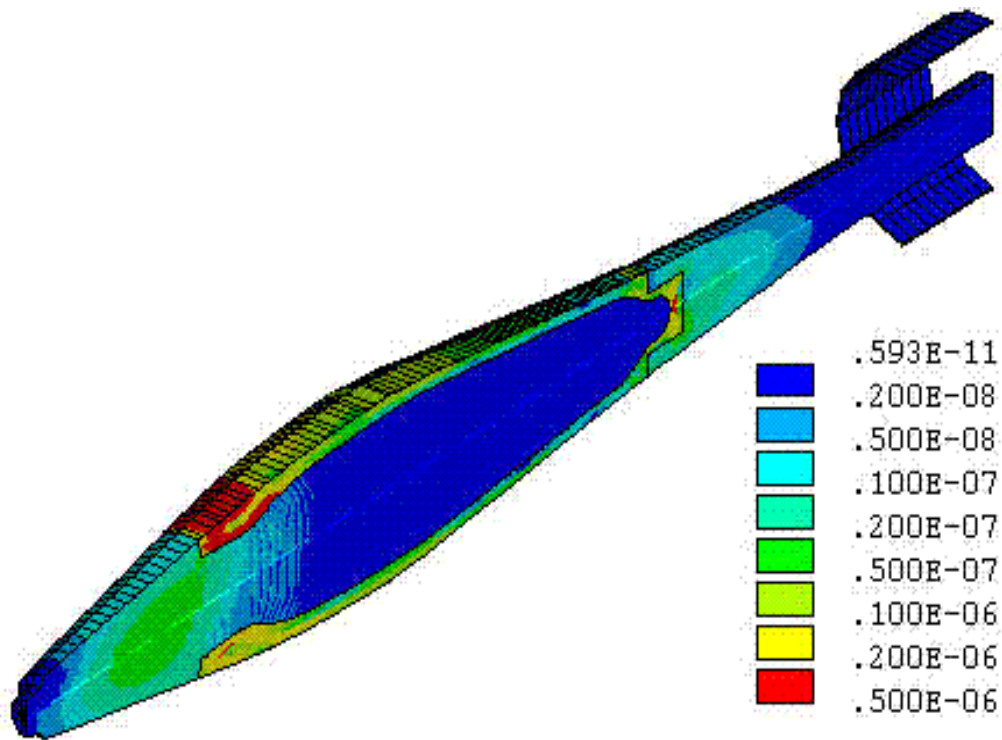


Figure 10. Magnetic induction in horizontal 81-mm projectile 9.6 ms after transmitter turnoff. Induction is again highest in body, now concentrated in upper fuze adapter.

For induction in nonpermeable objects, the location of maximum current density would be expected to control voltages observed in a receiver coil. However, a model of the 81-mm projectile without the tail-fin shroud showed very little difference in the predicted EMF from the model with the tail-fin shroud (Fig. 4). This is because decay of magnetic induction in the steel body, and not eddy currents in the aluminum fuze and tail, dominate the secondary magnetic fields. The decay of this induction is of course itself determined by the interaction of magnetic and electric fields according to the Faraday and Ampere laws. Eddy currents are therefore present, but amplification of the magnetic induction due to the twohundredfold increase in permeability allows those currents to be small. Observations of increased decay times in ferrous UXO were reported previously by *McNeill and Bosnar* (1996). However, it is not the magnetic fields from free decay of domains that is observed, but the controlled decrease due to continued eddy-current interaction.

When the projectile is oriented horizontally beneath the sensor, the overall response is similar, albeit at lower amplitude because the elongated body is minimally coupled to the primary field, in agreement with the computations for solid prolate ellipsoids above. Some asymmetries in field properties can be seen in this configuration. Eddy currents in the tail-fin shroud are asymmetrical in amplitude and reverse direction (Fig. 9): this is a degree 2 circulation in both angle and vertical position along the shroud. The magnetic induction is again highest in the steel body, but is concentrated on the upper side of the fuze adapter closest to the sensor.

Concluding Discussion

These calculations demonstrate the utility of the *ANSYS* finite-element program in computing the EM-induction response of arbitrary, ordnance-like objects. Future plans include explicit adaptation to the EM61-3D and EM63 (including computation of other spatial components), addition of nonaxisymmetric features, improved meshing and, of course, detailed comparisons with data. Even if computation times are reduced to some hours (many hours to a day is the norm now), it may still be impractical to generate the many states (position, depth, orientation) necessary to develop a pattern-recognition library of various ordnance. Instead, new models must be devised that can more efficiently approximate this behavior. The “mean-field theory” (MFT), under development for the last few years (*Weichman and Lavelly*, 2000), is one such approach. The MFT is based on the derivation of the eigenvalues (decay-time constants) and eigenvectors (current-circulation patterns) from a polynomial expansion of the electric field in the object of interest. It promises to be fast because these eigenstates can be precomputed and their subsequent relative excitation determined from the incident field. The theory is presently formulated for solid ellipsoids of revolution. The MFT and simpler theories for the sphere capture the low-order decay constants or poles for UXO because the steel portions are relatively simply shaped and dominate the sensor response. Extension of the MFT to hollow objects may be necessary for late-time (or low-frequency) measurements in which the eddy currents fully penetrate the shell.

A simple alternative model is to represent the object as a group of three orthogonal, time- or frequency-dependent dipoles (e.g., *Barrow and Nelson*, 1999; *Collins et al.*, 1999; *Pasion and Oldenberg*, 1998; *Bell et al.*, 2000). As long as the object is distant by more than about its own length from the transmitter coil, the dipole approximation is reasonable. The method requires a

number of EM measurements of each item of interest, but it appears to interpolate to intermediate states well. Additional complications are introduced by composite objects—additional sets of dipoles must be added (*Bell et al.*, 2000)—which could affect the uniqueness of the inverse problem. In the context of UXO discrimination, numerical calculations such as those presented here are most useful in developing new intuition for complex behaviors; such insights can guide the development of simpler analytic and empirical models.

Acknowledgements

Most of this work was funded by the U.S. Navy Explosive Ordnance Disposal Technology Division. Bill Bulat, formerly of Collaborative Solutions, Inc., performed the initial calculations and wrote the macros.

References

1. *ANSYS Theory Reference Release 5.5* (1998). P.L. Kohnke., Ed, ANSYS Inc.
2. Bell, T.H., B.J. Barrow, and J.T. Miller (2000). Subsurface discrimination using electromagnetic induction sensors. *IEEE Trans. Geosci. Remote Sens.*, in press.
3. Bulat, B., Dadkhah, Mahyar S., Schroeder, Scott A. (1998). 3D Induction Heating Simulation of a Helical Gear. 1998 ANSYS Conference Proceedings, vol. 2,.
4. Barrow, B.J., and H.H. Nelson (1999). Model-based characterization of EM induction signatures for UXO/clutter discrimination using the MTADS Platform. *UXO Forum 99*, Dept. of Defense Explosives Safety Board, Alexandria, VA, CD-ROM.
5. Collins, L., P. Gao, N. Geng, L. Carin, D. Keiswetter, and I.J. Won (1999). Discrimination of UXO-like metal targets using wideband electromagnetic induction. *UXO Forum 99*, Dept. of Defense Explosives Safety Board, Alexandria, VA, CD-ROM.
6. Grimm, R.E., M.W. Blohm and E.M. Lavelly (1997). UXO characterization using multicomponent, multichannel time-domain electromagnetic induction. *UXO Forum 97*, Dept. of Defense Explosives Safety Board, Alexandria, VA, 134-143.
7. Kaufman, A.A. (1978). Frequency and transient responses of electromagnetic fields created by currents in confined conductors. *Geophysics*, 43, 1002-1010.
8. Kaufman, A.A., and G.V. Keller (1985). *Inductive Mining Prospecting Part 1: Theory*, Elsevier, Amsterdam, 620 pp.
9. McNeil, J.D., and M. Bosnar (1996). Application of time domain electromagnetic techniques to UXO detection, *UXO Forum 96*, Dept. of Defense Explosives Safety Board, Alexandria, VA, 34-42.
10. Pasion, L.R., and D.W. Oldenburg (1998). Locating and determining dimensionality of UXOs using time domain electromagnetic induction. *UXO Forum 98*, Dept. of Defense Explosives Safety Board, Alexandria, VA, 763-772.
11. Weichman, P.B., and E.M. Lavelly (2000). Time domain scattering using the mean field approach, unpublished manuscript.